Scattering of Internal Waves at Finite Topography in Two Dimensions. Part II: Spectral Calculations and Boundary Mixing

PETER MÜLLER AND XIANBING LIU

Department of Oceanography, University of Hawaii at Manoa, Honolulu, Hawaii

ABSTRACT

The scattering of internal gravity waves at finite topography is studied theoretically and numerically for a two-dimensional finite-depth ocean. In Part I a single incident plane wave was considered. Here a random superposition of incident waves is considered with a spectrum derived from the Garrett and Munk spectrum. The topography is either a slope–shelf or ridge configuration with the bottom being flat in the far fields. The incident energy flux is partitioned into reflected and transmitted waves and redistributed in modenumber space. The scattering is irreversible. In frequency space topography acts like a filter. Waves with frequencies lower than the critical frequency are reflected. Waves with frequencies higher than the critical frequency are transmitted onto the shelf or across the ridge. In modenumber space, both the reflected and transmitted flux spectra are flatter than the incident spectrum, indicating a transfer from low to high modenumbers. This transfer is accompanied by an increase in the energy spectrum and, even more so, in the shear spectrum. A critical modenumber is determined such that the cumulative inverse Richardson number up to this modenumber is one. The flux scattered to modenumbers beyond this critical modenumber is calculated and is assumed to be available for internal wave induced boundary mixing. Various topographic profiles are compared. Convex profiles are more efficient than linear or concave profiles in scattering waves to high modenumbers.

1. Introduction

The scattering of internal waves at bottom topography redistributes the incident energy flux in physical and wavenumber space. This redistribution is theoretically studied for finite topography in a two-dimensional finite depth ocean. The consideration of finite topography and a finite depth ocean is a step toward more realism than previous studies, which considered infinitesimal topography or an infinite ocean without an upper surface (e.g., Phillips 1966; Baines 1971a,b; Eriksen 1982; Rubenstein 1988; Müller and Xu 1992). The two-dimensionality remains a major idealization.

In Müller and Liu (2000, hereafter Part I) we studied the energy flux redistribution for a single plane wave incident on either a slope–shelf or ridge configuration. The primary aim was to understand how the redistribution depends on the parameters of the incident wave, that is, its frequency and modenumber, and on the parameters of the topography, that is, its height, slope, and higher derivatives. In this paper we generalize the study to a random incident wave field with a Garrett and Munk spectrum (henceforth GM spectrum; Garrett and Munk 1972; Munk 1981). In addition to the flux redistribution we will also calculate the reflected and transmitted energy and shear spectra and inverse Richardson numbers. The ultimate aim of this part is to understand which topographic profiles are most efficient in transferring energy to high modenumber waves that are likely to break and cause boundary mixing.

Laboratory experiments have long established that internal waves reflecting off sloping boundaries can cause strong mixing near the boundary (e.g., Cacchione and Wunch 1974; Ivey and Nokes 1989). In the ocean, elevated internal wave energy and shear levels and boundary mixing have been found near continental slopes, ridges, and seamounts (e.g., Eriksen 1982, 1998). The basic dynamical argument for internal wave induced boundary mixing comes from the theory of internal wave reflection off a straight slope (Phillips 1966; Eriksen, 1982). When the slope becomes critical, the reflected wave has an infinite wavenumber and zero group velocity. The energy and shear increase beyond bound near the slope. The first attempt to quantify this mechanism is due to Eriksen (1985). He calculated the spectrum that results from reflecting an incident GM spectrum off an infinite straight slope. A significant fraction of the incident energy flux is redistributed in wavenumber space, mostly by near-critical reflection. Subsequently, Garrett and Gilbert (1988) determined a

Corresponding author address: Dr. Peter Müller, Department of Oceanography, University of Hawaii at Manoa, 1000 Pope Road, MSB 429, Honolulu, HI 96822.
E-mail: pmuller@iniki.soest.hawaii.edu

critical modenumber such that the cumulative inverse Richardson number from the lowest modenumber to the critical modenumber is one. They then argued that waves reflected to modenumbers higher than the critical modenumber are likely to break and cause mixing. They calculated the flux to these high modenumber breaking waves to be of the order of 1 mW m^{-2} and showed that this amount is sufficient to cause an effective basinwide mixing or vertical diffusion coefficient of the order of 10^{-4} m^2 s^{-1} in the deep ocean. In a companion paper, Gilbert and Garrett (1989) studied the scattering of a single plane wave incident from above onto curved topography, using Baines' (1971a,b) scattering theory. They found that convex topography is more efficient than concave topography in scattering waves to high wavenumbers. Here we continue this line of research and study the scattering of a wave spectrum incident from the side onto finite topography in a finite depth ocean.

The calculation of the energy flux scattered to high modenumbers is, of course, only the first step to assess internal-wave-induced boundary mixing. In addition one needs to analyze what fraction of the flux to high wavenumbers is dissipated and what fraction is used for mixing and converted to potential energy; how fast do secondary circulations replenish mixed boundary water and communicate the mixing to the interior; and how the scattering process is affected by friction, nonlinear interactions, refraction and other dynamical processes. These issues are far from resolved. Here we only consider the implications that can be drawn from the scattering process itself.

Drawing inferences for the real ocean from our calculations presents major problems. First of all, our calculations are two-dimensional. The topography is independent of one horizontal coordinate, say the y coordinate, and we only consider incident (and scattered) waves whose wavenumber components in y direction are zero. These waves have a horizontal group velocity normal to the topography. We do not know how representative our results are for waves propagating onto the topography from other horizontal directions. A second problem is that our theoretical approach requires an ocean with a constant Brunt–Väisälä (henceforth BV) frequency, both independent of depth and having the same value in the deep ocean and on the shelf. A possible generalization (Baines 1973) to a more general class of BV profiles is not pursued. The GM spectrum, on the other hand, is formulated for an ocean with an exponential BV profile. We thus face matching problems. These and other limitations are more fully discussed in the paper. Our basic approach is to compare the scattered field to the incident field and to compare different topographic profiles, assuming that these comparisons are less affected by our idealizations than are absolute values.

In section 2 we generalize the scattering theory developed in Part I to a random ensemble of incident waves and introduce energy flux, energy, and shear spectra. After these theoretical foundations, we specify in section 3 the incident wave spectrum by projecting the three-dimensional GM spectrum onto two dimensions. In section 4, we give some technical details about our suite of numerical calculations. The results of our calculations are discussed separately for the energy flux spectrum, the energy spectrum, and the inverse Richardson number. We start in section 5 with the energy flux spectrum. It most succinctly describes the scattering process since the energy flux obeys a conservation law. The incident flux is partitioned into a reflected and a transmitted flux and redistributed in modenumber space. The energy spectra are discussed in section 6. Section 7 calculates inverse Richardson numbers for all our topographic profiles. These inverse Richardson numbers are then used in section 8 to calculate critical modenumbers and the flux to high modenumber breaking waves. In the final section, we summarize and discuss our results.

2. Spectral theory

a. Scattering cross section

The scattering of internal waves at finite topography in two dimensions is governed by the wave equation

$$[N^2(z) + \partial_{tt}]\partial_{xx}\psi + (\partial_{tt} + f^2)\partial_{zz}\psi = 0, \qquad (1)$$

where $\psi(x, z, t)$ is the streamfunction, $N(z)$ the BV frequency, and f the Coriolis frequency. This wave equation must be solved for a prescribed incident wave field subject to the boundary conditions that $\psi = 0$ at the surface $z = 0$ (rigid lid approximation) and at the bottom $z = -h(x)$ and subject to the radiation condition that the scattered wave field must be an outgoing field. Since the scattering problem is time invariant, it can be solved for each frequency separately. We thus Fourier decompose the streamfunction

$$\Psi(x, z, t) = \int \Psi(x, z) \exp(-i\omega t) \, d\omega. \qquad (2)$$

The Fourier amplitudes $\Psi(x, z)$ then satisfy

$$\partial_{xx}\Psi - c^2(z)\partial_{zz}\Psi = 0, \qquad (3)$$

where

$$c(z) = \sqrt{\frac{\omega^2 - f^2}{N^2(z) - \omega^2}} \qquad (4)$$

is the wave slope. We assume $N = N_0 = $ const and hence $c = c_0 = $ const. The wave equation (3) then has the solution

$$\Psi = \sqrt{c_0}[f(\xi) + g(\eta)], \qquad (5)$$

where $f(\xi)$ and $g(\eta)$ are arbitrary functions of the characteristic coordinates ξ and η. These arbitrary functions have to be determined from the boundary and radiation

conditions. Baines (1973) showed that the solution (5) with c_0 replaced by $c(z)$ is also the solution for a more general class of BV frequencies. We do not pursue this possible generalization, regarding the two-dimensionality and linearity of the internal wave field as our major idealizations. We consider scattering at localized topography. A prescribed wave field Ψ^i is incident from the plus side. The total field in the far fields is then given by

$$\Psi_+ = \Psi_+^i + \Psi_+^s \tag{6a}$$

$$\Psi_- = \Psi_-^s, \tag{6b}$$

where $\Psi_+^s(\xi)$ is the backscattered or reflected field and $\Psi_-^s(\xi)$ the forwardscattered or transmitted field. Since the bottom is flat in the far fields, the incident, reflected, and transmitted fields can all be decomposed into vertical normal modes. In Part I, we derived an expression [Equation (21) of Part I] that relates the modal amplitudes $a_s^\pm(n, \omega)$ of the scattered field to the modal amplitude $a^i(m, \omega)$ of the incident wave. This expression can be rewritten as

$$a_s^\pm(n, \omega) = T_s^\pm(n, m, \omega)a^i(m, \omega), \tag{7}$$

where $T_s^\pm(n, m, \omega)$ is called the scattering cross section or response function. The scattering cross section determines how much of the incident modal amplitude at modenumber m and frequency ω is scattered to the reflected $(+)$ and transmitted $(-)$ modal amplitude at modenumber n and frequency ω. Scattering does not change the frequency. The scattering cross section depends on the variables indicated and, in addition, on the Coriolis and BV frequencies and, of course, on the topography. In Part I we described and discussed a numerical code that evaluates $T_s^\pm$ for arbitrary localized topography.

b. Spectral representation

Consider a superposition of incident waves

$$\Psi^i = \sum_n \int a^i(n, \omega)\sqrt{c_0}(e^{-ik_+\xi} - e^{-ik_+\eta}) \, d\omega, \tag{8}$$

where

$$k_+ = \frac{n\pi}{H_+}c_0 \tag{9}$$

is the horizontal wavenumber and H_+ is the ocean depth in the far field. The subscript $+$ indicates that these values are taken on the plus side. The signs in the exponentials of (8) assure that the wave field is an incident wave field with the energy flux vector or group velocity vector pointing toward the topography. For such a superposition the scattering formula (7) becomes

$$a_s^\pm(n, \omega) = \sum_m T_s^\pm(n, m, \omega)a^i(m, \omega). \tag{10}$$

Next assume that the incident wave field is an ensemble of statistically independent waves. Then

$$\langle a^i(n, \omega)a^i(n', \omega')\rangle = 0$$

$$\frac{k_+^2}{c_0}\langle a^i(n, \omega)a^{i*}(n', \omega')\rangle = E_i(\omega, n)\delta(\omega - \omega')\delta_{nn'}. \tag{11}$$

Here angled brackets indicate ensemble averages and $E(n, \omega)$ is the energy spectrum. It is normalized such that

$$\sum_n \int E(n, \omega) \, d\omega = E, \tag{12}$$

where

$$E = \frac{1}{2}(\langle u^2\rangle + \langle v^2\rangle + \langle w^2\rangle + N^2\langle \zeta^2\rangle) \tag{13}$$

is the total (kinetic plus potential) energy density. If we assume that the scattered waves are also statistically independent of each other, then (10) and (11) imply

$$E_s^\pm(n, \omega) = \left(\frac{H_+}{H_\pm}\right)^2 \sum_m |T_s^\pm(n, m, \omega)|^2 \left(\frac{n}{m}\right)^2$$

$$\times E_i(m, \omega). \tag{14}$$

The assumption that the scattered waves are independent is an important one. It is not strictly true for the solution (10). An incident mode is generally scattered into many modes, resulting in correlations between these scattered modes. However, in the real ocean, as these modes propagate away from the scattering region, they are affected by various processes that tend to decorrelate them. The statistical independence in the far field is thus a good physical assumption, an assumption that is almost always made when spectra are considered.

The assumption that the scattered waves decorrelate and become statistically independent in the far fields makes the scattering process irreversible. One expects that there exists an equilibrium solution and an H theorem. However, we were unable to prove this assertion. We neither have an explicit expression for the scattering cross section nor could we establish its general properties.

We are also interested in the shear spectrum

$$S(n, \omega) = \frac{k^2}{c_0^2}\left(1 + \frac{f^2}{\omega^2}\right)E(n, \omega), \tag{15}$$

which is normalized such that

$$\sum_n \int S(n, \omega) \, d\omega = \langle(\partial_z u)^2\rangle + \langle(\partial_z v)^2\rangle, \tag{16}$$

and in the vertically integrated energy flux spectrum

$$F(n, \omega) = \frac{H}{k}\frac{\omega^2 - f^2}{\omega}E(n, \omega), \tag{17}$$

which is normalized such that

$$\sum_n \int F(n, \omega) \, d\omega = \left| \int_{-H}^{0} dz \, \langle pu \rangle \right|. \quad (18)$$

For these spectra the scattering formula are

$$S_s^{\pm}(n, \omega) = \left(\frac{H_+}{H_\pm}\right)^4 \sum_m \left(\frac{n}{m}\right)^4 |T_s^{\pm}(n, m, \omega)|^2$$
$$\times S_i(m, \omega) \quad (19)$$

$$F_s^{\pm}(n, \omega) = \sum_m \frac{n}{m} |T_s^{\pm}(n, m, \omega)|^2 F_i(m, \omega). \quad (20)$$

Note that the BV frequency and all the spectra are independent of depth in this section.

3. Specification of incident spectrum

Our spectral calculations aim at assessing the efficiency of the scattering for real ocean conditions. We therefore want to specify the incident spectrum as the GM spectrum. This meets with two difficulties: First, the GM spectrum is formulated for a three-dimensional ocean, not for a two-dimensional one. Second, it is formulated for an exponential BV profile, not for a constant profile.

To deal with the first problem we consider the total energy flux onto the topography, integrated over all incident azimuthal directions, in a three-dimensional ocean. For each depth it is given by

$$F(n, \omega, z) = \int_{-\pi/2}^{\pi/2} E(n, \omega, \phi, z) c_g(n, \omega, z) \cos\phi \, d\phi,$$
$$(21)$$

where ϕ is the azimuthal angle, E the energy spectrum as a function of the indicated variables,

$$c_g = \frac{\omega^2 - f^2}{\omega} \frac{N^2(z) - \omega^2}{N^2(z) - f^2} \frac{1}{k(n, \omega)} \quad (22)$$

the magnitude of the horizontal group velocity, and $k = k(n, \omega)$ the dispersion relation. We next evaluate this flux for the GM spectrum making use of the fact that the GM spectrum is horizontally isotropic. We obtain

$$F_{GM}(n, \omega, z) = \frac{1}{\pi} E_{GM}(n, \omega, z) c_g(n, \omega, z) \quad (23)$$

where $E_{GM}(n, \omega, z)$ is the three-dimensional GM energy spectrum. If we assume that this azimuthally integrated energy flux is carried by a two-dimensional wave field, then this two-dimensional field must have the energy spectrum

$$E_{GM}^{2D}(n, \omega, z) = \frac{1}{\pi} E_{GM}(n, \omega, z). \quad (24)$$

It differs from the three-dimensional spectrum only by the factor $1/\pi$. If we assume that only a fraction α of the azimuthally integrated flux is carried by two-dimensional waves then a factor α will appear on the right hand side of (24). We will not assert any specific value of α. The interpretation of our calculations will not be based on absolute values of the scattered spectra but on relative values, relative to the incident spectra, and these relative values are independent of α.

The GM spectrum scales with depth as

$$E_{GM}(n, \omega, z) = b^2 N(0) N(z) E_{GM}(n, \omega), \quad (25)$$

where $N(z) = N(0)e^{-z/b}$ with $N(0) = 5.2 \times 10^{-3}$ s^{-1} and $b = 1.3$ km is the GM stratification and where $E_{GM}(n, \omega)$ is the normalized GM spectrum, given explicitly in the appendix. To deal with the second problem, namely that our scattering theory is formulated for a constant BV profile, we assume that the incident spectrum in the scattering formula (14) is given by the two-dimensional GM spectrum at a depth $z = z_0$ where $N(z_0) = N_0$. Thus

$$E_i(n, \omega) = \frac{1}{\pi} b^2 N(0) N_0 E_{GM}(n, \omega). \quad (26)$$

These specifications imply that waves from all azimuthal directions and all depths scatter as if coming from one direction and one depth. We choose $N_0 = 15f$, which corresponds to $z_0 = 2$ km for $f = 7.3 \times 10^{-5}$ s^{-1} (lat = 30°). The scattered spectra $E_s^{\pm}(n, \omega)$ in the deep ocean, not on the shelf, are also interpreted as the scattered spectra at depth z_0. This allows for a meaningful comparison with the incident spectrum.

The shear spectrum associated with the two-dimensional GM spectrum (24) is obtained from a generalization of the kinematic relation (15) to a depth-dependent BV frequency and from the GM dispersion relation

$$k(n, \omega) = \frac{n\pi}{b} \sqrt{\frac{\omega^2 - f^2}{N^2(0) - \omega^2}}. \quad (27)$$

The result is

$$S_{GM}^{2D}(n, \omega, z) = \pi N(0) N(z) \left[1 + \left(\frac{f}{\omega}\right)^2\right] \frac{N(z)^2 - \omega^2}{N^2(0) - \omega^2}$$
$$\times n^2 E_{GM}(n, \omega). \quad (28)$$

This shear spectrum at a depth z_0 where $N(z_0) = N_0$ will be used as the incident spectrum

$$S_i(n, \omega) = S_{GM}^{2D}(n, \omega, z_0) \quad (29)$$

in the scattering formula (19). In the deep ocean, we again interpret the scattered spectrum as the spectrum at depth z_0.

Similarly, we use

$$F_i(n, \omega) = \int_{-H_+}^{0} F_{GM}(n, \omega, z) \, dz$$
$$\simeq N^2(0) \frac{b^4}{n\pi^2} \frac{\sqrt{(\omega^2 - f^2)(N^2(0) - \omega^2)}}{\omega}$$
$$\times E_{GM}(n, \omega) \quad (30)$$

as the incident flux spectrum in the scattering formula (20). Equation (30) is correct to order $f/N(0)$.

We specify three incident spectra, E_i, S_i, and F_i, and use three scattering formulas, (14), (19), and (20), to calculate the scattered spectra. We could alternatively calculate the scattered shear and flux spectra from the scattered energy spectrum, using the kinematic relation (15) and (17) or generalizations of them. It is then, however, not obvious with which incident shear and flux spectra these scattered spectra should be compared. In any case, our approach is one way of dealing with the limitations of our scattering theory.

4. Numerical calculations
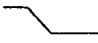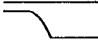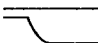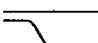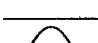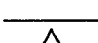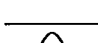
Here we describe the set-up of our numerical calculations. As in Part I we consider the scattering at two topographic configurations: a slope–shelf configuration with the wave field incident from the deep ocean side and a ridge configuration. The specific topographic profiles are the same as in Part I and are listed in Table 1, together with some pertinent parameters. The ridge profiles are obtained by mirroring the slope profiles. For each profile the depth ratio

$$\delta = \begin{cases} \dfrac{H_-}{H_+} & \text{for slope-shelf configuration} \\ \dfrac{H_+ - d}{H_+} & \text{for ridge configuration} \end{cases} \quad (31)$$

takes on the eight different values: 1/32, 2/32, 4/32, 8/32, 12/32, 16/32, 20/32, and 24/32. The width of the profile is adjusted as to keep the maximum slope at the value indicated in the table. In (31) d is the height of the ridge.

The scattering cross sections $T_s^{\pm}(n, m, \omega)$ are numerically evaluated on a grid, using the code described in Part I. The code is based on a mapping function which is obtained by tracing characteristics. There are 76 frequency points with the resolution decreasing from the Coriolis frequency $f = 7.3 \times 10^{-5}$ s^{-1} (lat = 30°) to the frequency $\omega = 10f$. The incident modenumbers run from $m = 1$ to $m = 60$, the scattered modenumbers from $n = 1$ to $n = M$ where $M = 256$ or 512 as indicated in Table 1. The maximum incident modenumber is limited to $m = 60$ since higher modes are not likely to propagate the distances envisioned by our scattering theory without being severely affected by nonlinear and dissipative processes (D'Asaro 1991). The range of the scattered modenumber is larger, not because we are interested and believe in the detailed structure of the spectra at high modenumbers, but to reduce aliasing effects on low modenumbers. Indeed we will display scattered spectra only up to modenumber $n = 60$ as well. All calculations were carried out on a SPARC Enterprise 300 workstation with two processors. The calculation of one scattered spectrum required about 2 h of CPU time if $M = 512$.

TABLE 1. Topographic configurations for which numerical calculations have been performed. All cases were run for the eight depth ratios 1/32, 2/32, 4/32, 8/32, 12/32, 16/32, 20/32, and 24/32 and for 76 frequencies between f and $\omega = 10f$, and for incident modenumbers $n = 1$ to 60. The width of the topographic profiles is adjusted to keep the maximum slope at the given value.

Topography	Maximum slope	Truncation modenumber
Linear slope	0.02	256 or 512
Parabolic convex slope	0.04	256 or 512
Parabolic concave slope	0.04	512
Cosine slope	0.0314	512
Triangular ridge	0.02	256 or 512
Parabolic convex ridge	0.04	512
Parabolic concave ridge	0.04	512
Cosine ridge	0.0314	512

As discussed in Part I, the scattering only depends on certain dimensionless parameters such as the depth ratio and normalized bottom slope. A particular important distinction had to be made between supercritical topography, where the maximal topographic slope exceeds the wave slope, and subcritical topography, where the maximal topographic slope is less than the wave slope. For our spectral calculation we consider a given topography. A given topography is supercritical if the frequency is smaller than the critical frequency

$$\omega_c^2 = N_0^2 \frac{h_{\max}'^2}{1 + h_{\max}'^2} + f^2 \frac{1}{1 + h_{\max}'^2}, \quad (32)$$

where $h_{\max}'$ is the maximum slope of the topography. It is subcritical if $\omega > \omega_c$. Often frequencies $\omega > \omega_c$ are called supercritical frequencies and frequencies $\omega < \omega_c$

subcritical frequencies. Thus supercritical frequencies imply subcritical topography and vice versa. To avoid confusion we will only use the adjectives ''subcritical'' and ''supercritical'' in conjunction with topography. For typical topographic slopes the critical frequency is quite close to f. For $h' = 0.02$ one finds $\omega_c = 1.05 f$.

In Part I we discussed the dependencies of the scattering process on parameters like the incident modenumber, the depth ratio, the maximum normalized slope, and higher derivatives of the topography. For an incident wave spectrum one has to sum over all incident modenumbers. This leads to a smoothing with generally less dramatic dependencies.

5. Redistribution of energy flux

The scattering process is most succinctly described by the vertically integrated energy flux since it obeys for each frequency the conservation law

$$\sum_m F_i(m, \omega) = \sum_n F_s^+(n, \omega) + \sum_n F_s^-(n, \omega). \quad (33)$$

This law is a consequence of energy conservation for the scattering process and a generalization of (27) in Part I to a superposition of incident waves. The incident energy flux is partitioned into reflected and transmitted waves and redistributed in modenumber space. However, because we truncate the summation over n at $M = 256$ or 512 in our numerical calculations and at $n = 60$ in our figures, the reflected and transmitted fluxes might not always add up to the incident flux. The difference is being scattered to modenumbers not resolved by our numerical calculation or not displayed in our figures.

The total energy flux incident onto the topography is

$$F_i = \int_f^N \sum_m F_i(m, \omega) \, d\omega. \quad (34)$$

For the two-dimensional GM spectrum (30) and our parameter choices we find the numerical value

$$\rho F_i = \rho \times 0.59 \text{ m}^4 \text{ s}^{-3} = 590 \text{ W m}^{-1}, \quad (35)$$

where ρ is the density of water. Note that this is a vertically integrated horizontal energy flux. A typical local horizontal flux is obtained by dividing by the ocean depth and is of the order of 100 mW m^{-2}. This value is an order of magnitude larger than the local vertical energy flux. A vertical diffusivity $K_v = 10^4$ m^2 s^{-1} requires a vertical energy flux of about 1 mW m^{-2} or a horizontal flux of about about 20 mW m^{-2} for $h' = 0.05$ (Garrett and Gilbert 1988).

Figure 1 shows the incident, reflected and transmitted energy flux as a function of frequency and modenumber for a half-cosine slope of depth ratio $\delta = 4/32$ and maximum slope $h'_{max} = 0.01\pi$. Overall, 91.4% of the incident flux is transmitted onto the shelf and 8.6% is reflected back to the ocean. To see more clearly how this partition occurs, consider first the frequency spectra

(a) Incident flux spectrum, half–cosine slope
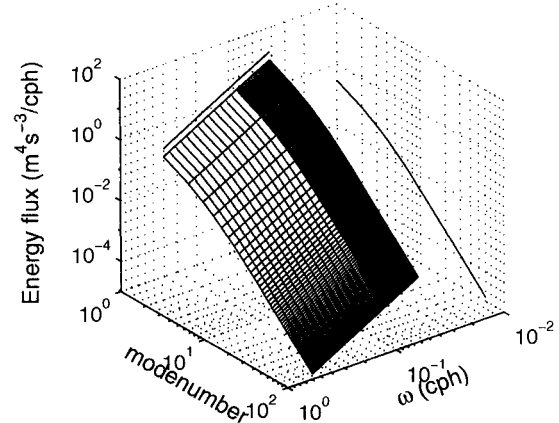
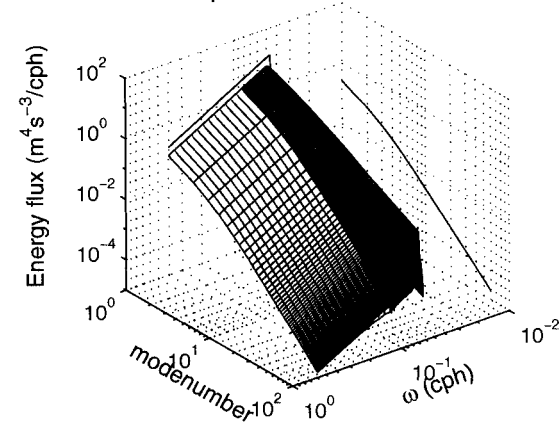(b) Reflected flux spectrum
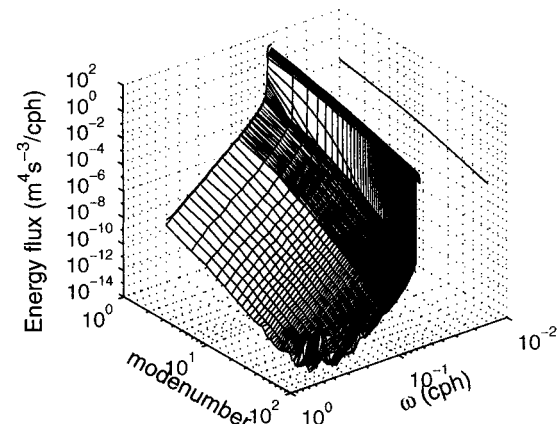
(c) Transmitted flux spectrum

FIG. 1. Incident, reflected, and transmitted flux spectra as a function of modenumber and frequency for a half-cosine slope of depth ratio $\delta = 4/32$ and maximum slope $h'_{max} = 0.01\pi$. Solid lines in the coordinate planes are the frequency and modenumber spectra.
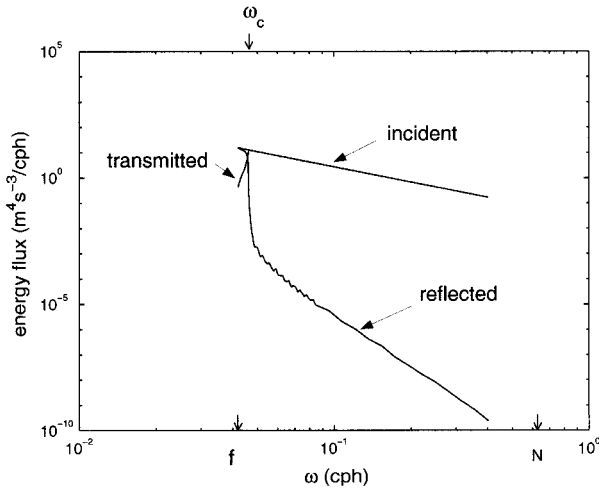
FIG. 2. Incident, reflected, and transmitted flux frequency spectra for the half-cosine slope of Fig. 1.

FIG. 3. Incident, reflected, and transmitted flux modenumber spectra for the half-cosine slope of Fig. 1.

$$F(\omega) = \sum_n F(n, \omega),　(36)$$

which satisfy

$$F_i(\omega) = F_s^+(\omega) + F_s^-(\omega).　(37)$$

Figure 2 shows these frequency spectra. The incident GM spectrum has a -2 slope. For frequencies $\omega > \omega_c$, most of the flux is transmitted onto the shelf. For frequencies $\omega < \omega_c$, most of the incident flux is reflected back to the deep ocean. The topography thus acts like a filter in frequency space.

The modenumber spectra

$$F(n) = \int_f^{N_0} F(n, \omega)\, d\omega　(38)$$

satisfy

$$\sum_n F_i(n) = \sum_n F_s^+(n) + \sum_n F_s^-(n)　(39)$$

and are shown in Fig. 3. The incident spectrum has a -1 slope up to about $n = 3$ and a -3 slope beyond. The transmitted spectrum is very similar to the incident spectrum, just a little less at low modenumbers and a little higher at high modenumbers. The reflected spectrum has a lower overall level than the incident spectrum but a flatter shape. It also exceeds the incident spectrum at high modenumbers. These features indicate a transfer from low to high modenumbers, both for the reflected and transmitted fluxes.

The energy transfers are seen more clearly in Fig. 4 which shows the redistributed energy flux

$$D(n, \omega) = \begin{cases} F_s^-(n, \omega) - F_i(n, \omega) & \text{for } k_x < 0 \\ F_s^+(n, \omega) & \text{for } k_x > 0, \end{cases}　(40)$$

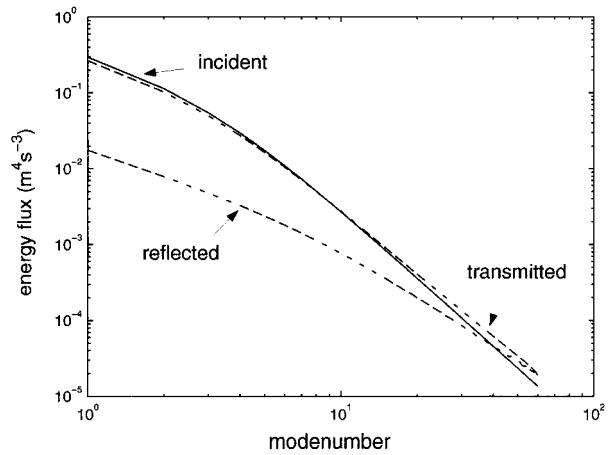where $k_x < 0$ indicates leftward and $k_x > 0$ rightward propagating waves. The redistribution is only significant for frequencies less than the critical frequency, that is, for frequencies for which the topography is supercritical. The major redistribution is from low modenumber leftward propagating waves to low and medium modenumber rightward propagating waves. There is also a transfer from low to medium modenumber leftward propagating waves for near-critical frequencies. The total redistributed energy flux, defined as the integral over the negative (or positive) lobe, is 8.9% of the incident flux. The flux to high modenumber waves that are likely to break will be calculated in section 8. Note that we display modenumber spectra. A given modenumber corresponds to a larger vertical wavenumber on the shelf than in the deep ocean.

The flux redistribution depends in a predictable manner on the depth ratio. For a half-cosine slope with a depth ratio of $\delta = \frac{1}{2}$ (with the same maximum slope
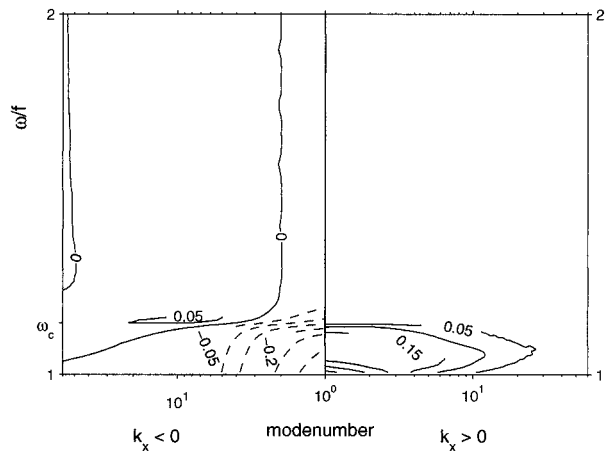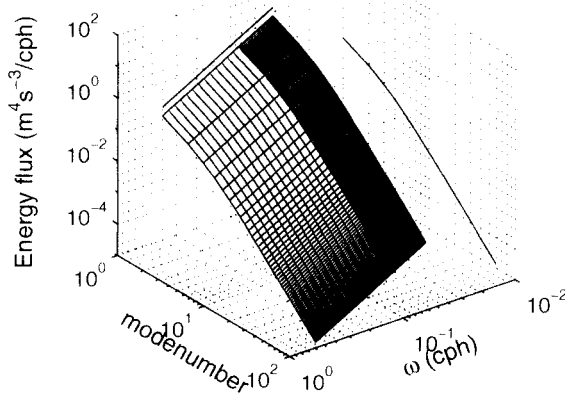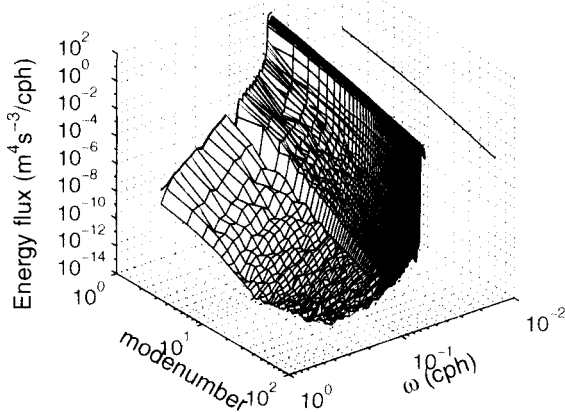

FIG. 4. Redistributed energy flux for the half-cosine slope of Fig. 1. The representation is variance conserving. For each frequency the positive and negative contributions should add up to zero. The total redistributed energy flux is defined as the integral over the negative (or positive) lobe.

(a) Incident flux spectrum, cosine ridge

(b) Reflected flux spectrum
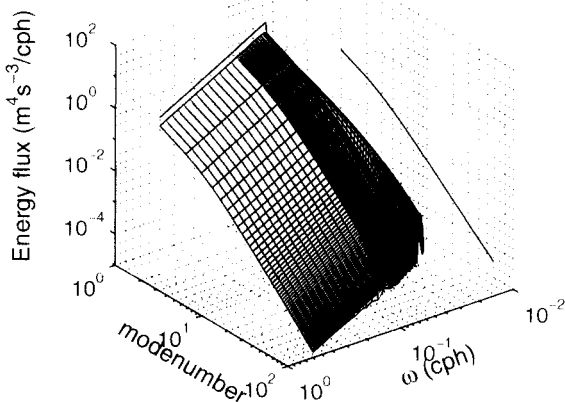

(c) Transmitted flux spectrum

FIG. 5. Incident, reflected, and transmitted flux spectra as a function of modenumber and frequency for a cosine ridge of depth ratio $\delta = 4/32$ and maximum slope $h'_{max} = 0.01\pi$. Solid lines in the coordinate planes are the frequency and modenumber spectra.
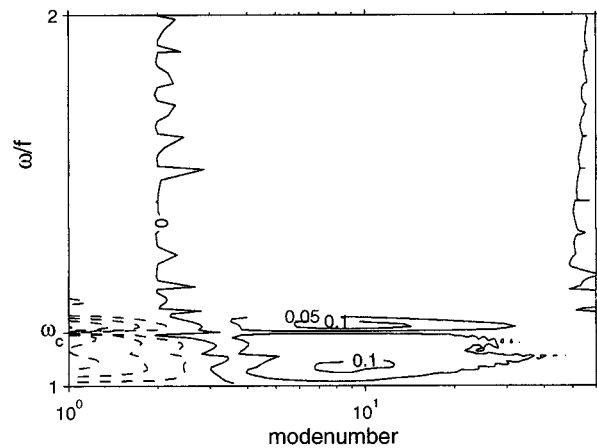

FIG. 6. Redistributed energy flux for the cosine ridge of Fig. 5. The representation is variance conserving. For each frequency the positive and negative contributions should add up to zero. The total redistributed energy flux is defined as the integral over the negative (or positive) lobe.

of $h'_{max} = 0.01\pi$ and, hence, the same critical frequency) more of the total incident energy flux is transmitted onto the shelf, namely 94.66%. Also, less of the flux is redistributed, only 7.28%. A deeper shelf is less of an obstacle.

The results for a ridge configuration are very similar to those for the slope–shelf configuration, for reasons more fully explained in Part I. Figure 5 shows the reflected and transmitted modenumber–frequency spectrum for a cosine ridge with a depth ratio $\delta = 4/32$ and maximum slope $h'_{max} = 0.01\pi$, the same values as for the slope-shelf configuration in Fig. 1. The only noticeable difference to Fig. 1 is a trench in the reflected spectrum at around $\omega = 0.1$ cph. The trench reflects nearly full transmission onto the shelf at this frequency because the mapping function becomes nearly linear for this frequency (see Part I for a discussion of this phenomenon). The trench has, however, little overall significance. It does not even noticeably raise the transmitted spectrum at that frequency.

For a ridge configuration we may consider the symmetric situation that a GM spectrum is incident from both sides. The redistributed energy flux is then given by

$$D(n, \omega) = F_s^+(n, \omega) + F_s^-(n, \omega) - F_i(n, \omega) \quad (41)$$

for both leftward and rightward propagating waves, and is shown in Fig. 6. The energy flux is redistributed from low to medium modenumbers at low and near-critical frequencies.

The redistribution

$$D(n) = \int D(n, \omega) \, d\omega \quad (42)$$

in modenumber space (Fig. 7) shows more succinctly that the energy flux is redistributed from the first and
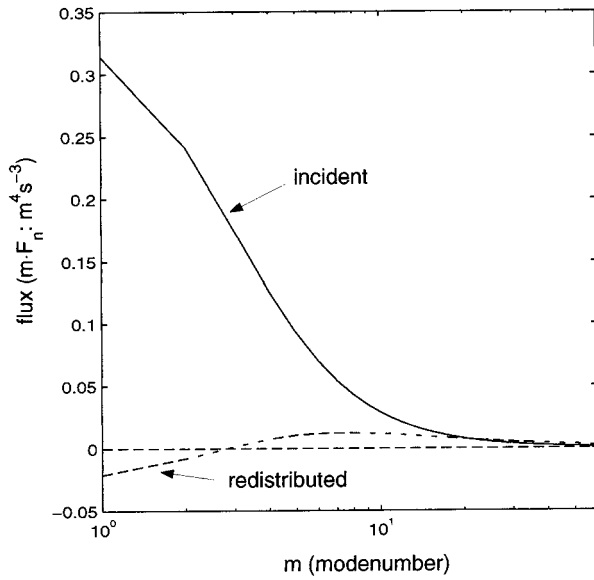
FIG. 7. Redistributed energy flux in modenumber space for the cosine ridge of Fig. 5. The representation is variance conserving. The positive and negative lobes should add up to zero.

second mode to modenumbers around $n = 10$. In total, 4.26% of the incident flux is redistributed. A maximum value of 7.6% is found for a depth ratio of $\delta = 20/32$.

6. Energy spectra

The energy spectra for the reflected and transmitted waves are calculated from the scattering formula (14). However, their basic features can be inferred from the kinematic relation

$$E(n, \omega) = \frac{F(n, \omega)}{c_\pm(n, \omega)} \qquad (43)$$

with the group velocity

$$c_\pm = \frac{\sqrt{\omega^2 - f^2}}{\omega} \frac{(N_0^2 - \omega^2)^{3/2}}{N_0^2 - f^2} \frac{H_\pm}{n\pi}. \qquad (44)$$

The group velocity approaches zero as the frequency approaches the Coriolis frequency. This amplifies the energy spectrum near the Coriolis frequency. Indeed, the GM energy spectrum has an integrable singularity at $\omega = f$. The group velocity also approaches zero as the modenumber increases. This amplifies the energy spectrum at high modenumbers. Finally, the group velocity is proportional to the ocean depth (if modenumber is used as a variable). This amplifies the energy spectrum on the shelf. We see all these amplifications effects in Figs. 8–10, which show the energy spectra corresponding to the flux spectra shown in Figs. 1–3.

The transmitted energy spectra are larger overall than the incident spectrum. The transmitted frequency spectrum shows a peak at the critical frequency ω_c. Reflection at an infinite straight slope predicts

(a) Incident energy spectrum, half cosine slope
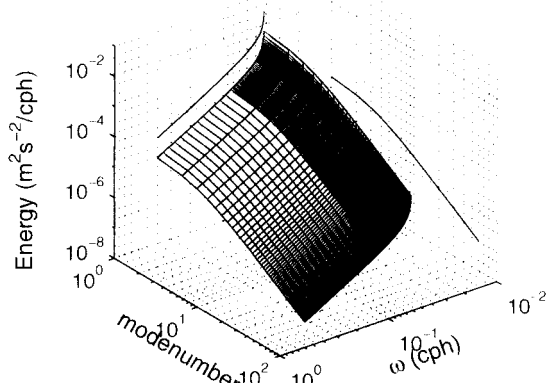
(b) Reflected energy spectrum
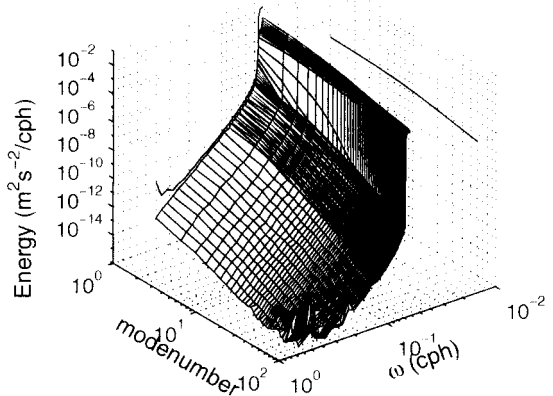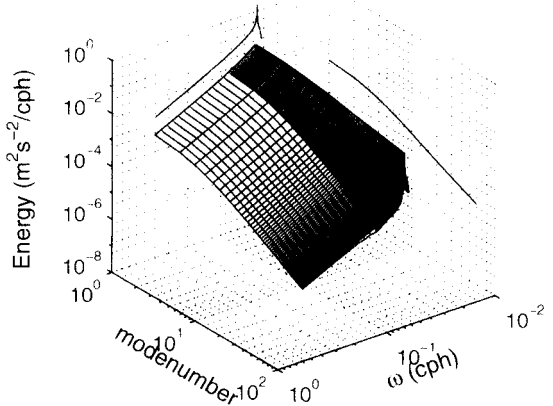

(c) Transmitted energy spectrum

FIG. 8. Incident, reflected, and transmitted energy spectrum as a function of modenumber and frequency for the half-cosine slope of Fig. 1.
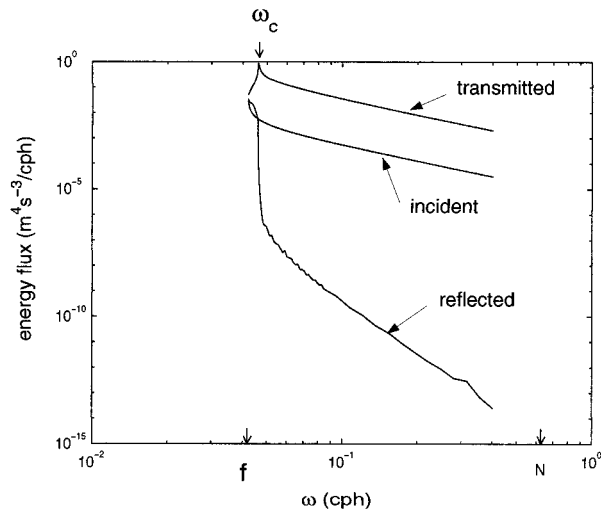
FIG. 9. Incident, reflected, and transmitted energy frequency spectra for the half-cosine slope of Fig. 1.

FIG. 10. Incident, reflected, and transmitted energy modenumber spectra for the half-cosine slope of Fig. 1.

$$\frac{E_r}{E_i} = \left(\frac{m_r}{m_i}\right)^2, \qquad (45)$$

where m is the vertical wavenumber. At the critical frequency, m_r approaches infinity and the reflected energy density thus approaches infinity as well. The scattering formula (14) shows the same dependence on modenumber as (45) and scattering at finite curved topography also leads to (integrable) singularities whenever a characteristic encounters a critical point on the topography, that is, a point where the wave slope equals the topographic slope (Baines 1971b). However, our numerical calculations do not capture any singular behavior at high modenumbers since they only resolve scattered modenumbers up to $M = 256$ or $M = 512$. The finiteness of the peak at ω_c in Fig. 9 is thus a consequence of our numerical procedure. Theretically, the singularities can be removed by considering an initial value problem or by including friction.

The reflected frequency spectrum is larger than the incident spectrum at near-inertial frequencies. The reflected modenumber spectrum is larger than the incident spectrum at high modenumbers.

7. Richardson number

Whenever energy is scattered to high modenumbers, the shear increases. The reflection laws at an infinite straight slope predict

$$\frac{S_r}{S_i} = \left(\frac{m_r}{m_i}\right)^4. \qquad (46)$$

The scattering formula (19) shows the same dependence when expressed in terms of modenumber and depth
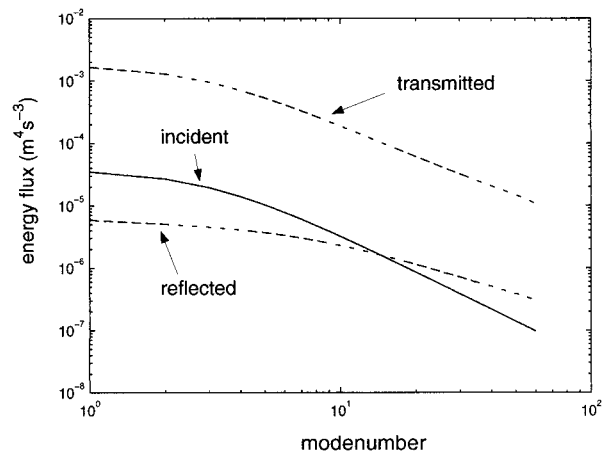
$$\frac{S_s^{\pm}}{S_i} = \left(\frac{H_+}{H_{\pm}}\right)^4 \left(\frac{n}{n_i}\right)^4. \qquad (47)$$

Compared to the waves reflected back to the deep ocean, waves transmitted onto the shelf experience an additional shear increase $(H_+/H_-)^4$ since the mode is squeezed into a shallower water column. Because of the power 4, these increases can be quite dramatic. Higher shears make the wave field more susceptible to shear instability and subsequent breaking and mixing. To assess this shear increase quantitatively we follow Munk (1981) and introduce the inverse Richardson number

$$\mathrm{Ri}^{-1} = \sum_n \int \frac{S(n, \omega)}{N_0^2} \, d\omega. \qquad (48)$$

The inverse Richardson number for the GM spectrum is order one. Our incident spectrum, extending only to modenumber 60, has an inverse Richardson number of only 0.007, two orders of magnitude smaller.

The inverse Richardson number of the scattered fields are obtained by summing all $M = 256$ or 512 resolved modes. The resulting values are lower bounds. The scattering to higher nonresolved modenumbers and the scattering from higher incident modenumbers are not considered. In the following we present the ratio of the scattered to the incident inverse Richardson number, which represents an amplification factor. Figure 11 shows the amplification factor for a half-cosine slope and a cosine ridge as a function of the depth ratio δ, both for reflected and transmitted waves. The GM spectrum is incident from only one side for the ridge configuration. The amplification factors are largest for the wave field transmitted onto the shelf, because of the "squeezing effect" (47) (note the logarithmic scale in the lower panel of Fig. 11). The amplification factors for the reflected waves are approximately the same for the slope and ridge case. Amplification factors of 100 and larger imply inverse Richardson numbers larger than 1. Thus, even leaving out the higher modenumber
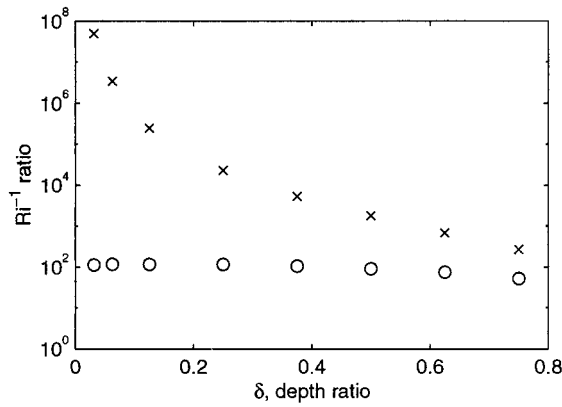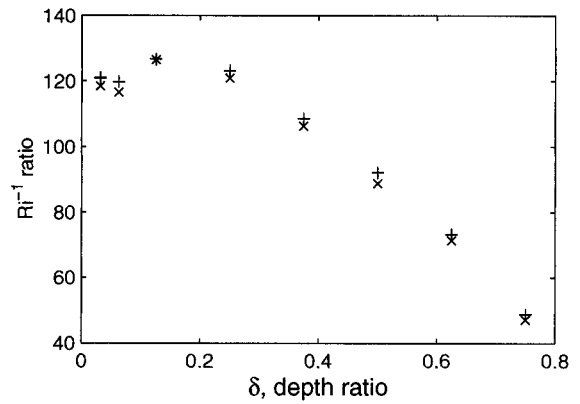
cosine ridge
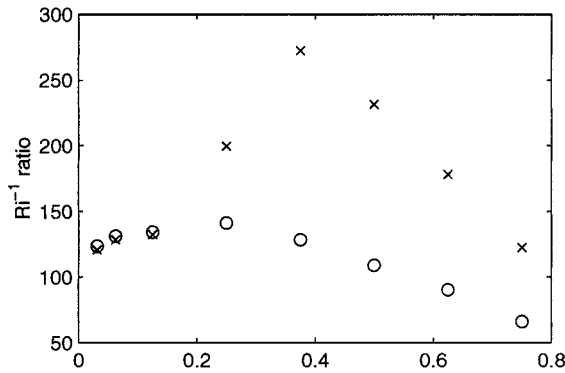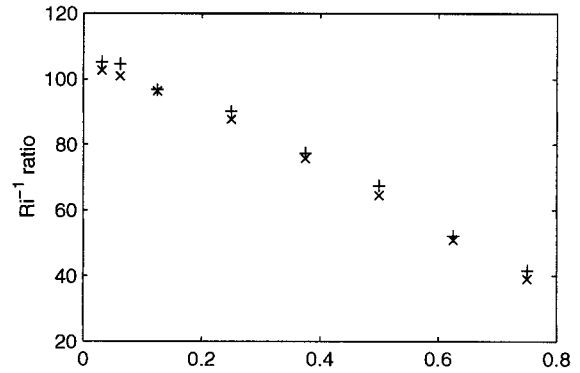
half–cosine slope

o: reflected wave, x: transmitted wave

FIG. 11. Inverse Richardson number ratios or amplification factors for half-cosine slopes and cosine ridges as a function of depth ratio.

Reflected waves

Transmitted waves

+: 256 resolved modes, x: 512 resolved modes

FIG. 12. Inverse Richardson number ratios or amplification factors for a triangle ridge as a function of depth ratio. Two calculations are compared, one with 256 resolved modes and one with resolved 512 modes. In both cases the inverse Richardson number is calculated from the first 256 modes.

incident waves, the scattering at these topographies results in wave fields that are likely to break and cause mixing. The figure also shows how the amplification factors depend on the depth ratio. In the ridge case, they first increase and then decrease with increasing depth ratio. The maximum is achieved at $\delta = 8/32$ for the reflected waves and at $\delta = 12/32$ for the transmitted waves.

The shear gets most of its contributions from high modenumbers. It is therefore the quantity that should be most susceptible to aliasing errors caused by our truncation of the scattered modenumber. Figure 12 shows, however, that aliasing is not a problem. It compares the inverse Richardson numbers or amplification factors calculated from the first 256 modes for two calculations, one with 256 resolved modes and one with 512 resolved modes. No major differences are apparent.

In Part I we showed that the fraction of the energy

flux that is scattered to high modenumbers depends on the topographic profile. Most importantly, convex profiles are more efficient than concave profiles; profiles with sharp corners are more efficient than smooth profiles. These dependencies, of course, carry through to the spectral calculations and inverse Richardson numbers. Figures 13 and 14 show the amplification factors for our different profiles. The results for the reflected waves are the cleanest, both for the slope and ridge configuration. The convex profiles give the highest amplification factors, followed by the linear profiles, followed by the cosine profiles, and the concave profiles give the lowest factors, for all values of the depth ratio. The high values for the convex profiles are not only due to the fact that they are more efficient in scattering waves to high modenumbers but also to the fact that they have
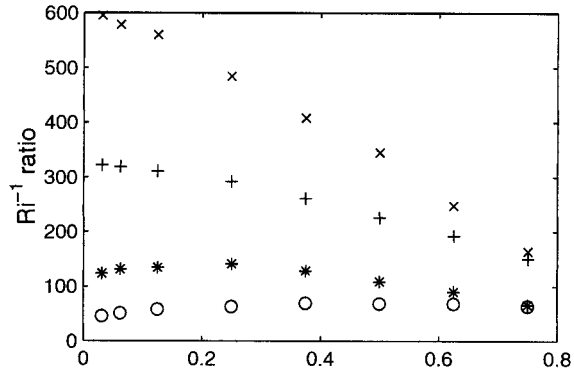
Reflected waves
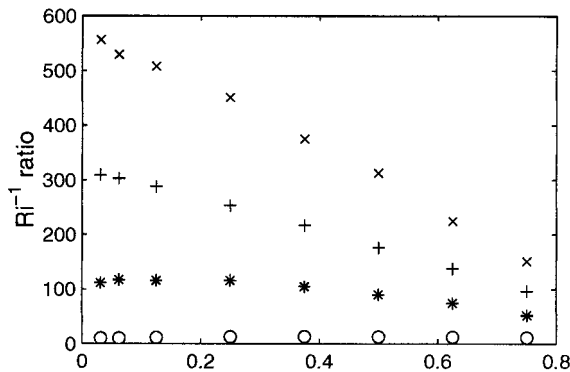
Transmitted waves
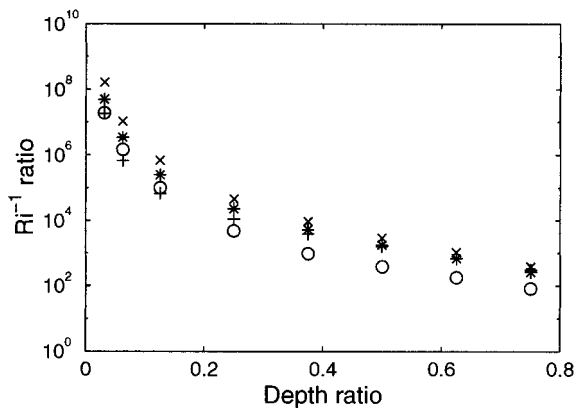
+: linear, x: convex, o: concave, *: cosine

FIG. 13. Inverse Richardson number ratios or amplification factors for various slope–shelf profiles as a function of depth ratio.

Reflected waves

Transmitted waves

+: linear, x: convex, o: concave, *: cosine

FIG. 14. Inverse Richardson number ratios or amplification factors for various ridge profiles as a function of depth ratio.
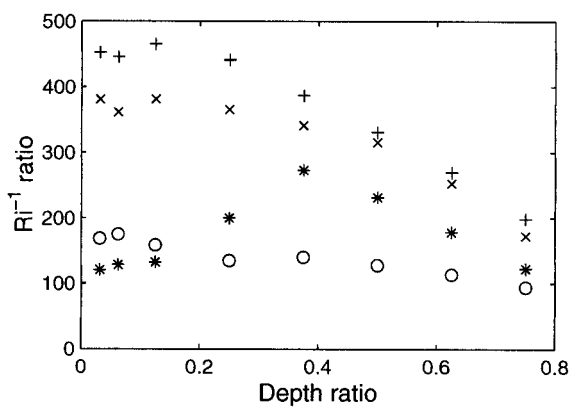
a higher maximum slope and hence critical frequency than the linear slopes. Thus more waves encounter supercritical slopes and get backreflected. The amplification factors for both the convex and linear profiles decrease with increasing depth ratio. The factors for the concave profiles increase slightly. The factors for the cosine profiles, which are convex at the top and concave at the bottom, lie indeed between the convex and concave profiles.

The results are more complex for the transmitted waves. In the ridge case, the linear profiles have the highest amplification factor, closely followed by the convex profiles. The cosine profiles have the lowest amplification factors at small depth ratios, the concave profiles at large depth ratios. The amplification factors for the waves transmitted onto the shelf are all larger because of the "squeezing effect." The convex profiles have the largest values.

8. Energy flux available for mixing

While the shear and inverse Richardson number are good indicators of the stability of the wave field, estimates of the internal wave induced boundary mixing and diffusion coefficients require the energy flux to high modenumber breaking waves (Garrett and Gilbert 1988). This energy flux is partly dissipated into heat and partly used for mixing, increasing the potential energy of the water column. From the rate of potential energy increase one can infer a diffusion coefficient. Here we calculate this flux following Garrett and Gilbert (1988) by first calculating a critical modenumber n_c such that the cumulative inverse Richardson number up to this modenumber is one,

$$\text{Ri}^{-1} = \sum_{n=1}^{n_c} \int \frac{S(n, \omega)}{N_0^2} \, d\omega = 1, \qquad (49)$$

and then calculating the energy flux to modenumbers beyond n_c. Because of our various assumptions this cal-

Critical modenumber

Energy flux scattered to modenumbers higher than n_c

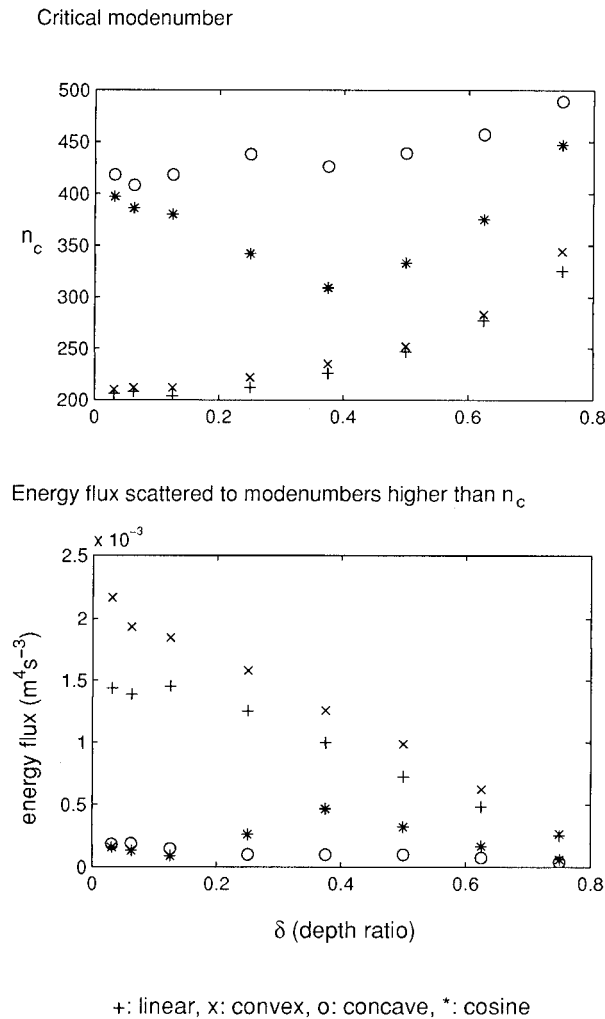+: linear, x: convex, o: concave, *: cosine

FIG. 15. Critical modenumber n_c and energy flux to modenumbers higher than the critical modenumber for various ridge profiles as a function of depth ratio. The GM spectrum is incident from both sides.

culation will again give lower bounds. Again our interest is mainly in the comparison of different profiles.

The results for the ridge configuration are shown in Fig. 15. The GM spectrum is incident from both sides. The upper panel shows the critical modenumber n_c as a function of the depth ratio δ for our four profiles. The concave profiles have the highest critical modenumbers, the linear and convex profiles the lowest critical modenumbers; the cosine profiles lie in between. The lower panel shows the energy flux scattered to modenumbers beyond n_c. The largest fluxes are obtained for the convex profiles, followed by the linear profiles. The concave and cosine profiles give the lowest values. Numerically, we obtain depth integrated values of up to 2×10^{-3} m^4 s^{-3} or 2 W m^{-1}. This corresponds to local values of the order of 0.4 mW m^{-2}, much smaller than the "required" value of 20 mW m^{-2}. Note, however, that our values are lower bounds. Overall, the fluxes show the same behavior as the inverse Richardson numbers in Fig. 14.

For the slope configuration, most of the transmitted energy flux is scattered to modenumber larger than n_c, as a consequence of the "squeezing effect." For the reflected field, the fluxes scattered beyond n_c are smaller than those for the ridge configurations shown in Fig. 15, because the contributions from the other side are missing.

9. Discussion and conclusions

We calculated the scattering of an incoming random internal wave field at slope–shelf and ridge configurations with various profiles. We specified the incident wave field to have a Garrett and Munk spectrum, to be realistic. However, realism is reduced by other idealizations that we made. They are reiterated here to put our results in perspective.

The first idealization is the two-dimensionality. For many slopes and ridges, two-dimensionality is a fair first approximation; for other topographic features like seamounts, it is clearly not. The oceanic internal wave and the GM spectrum are horizontally isotropic. Here, two-dimensionality implies that waves incident from all horizontal directions behave as if incident normal to the topography.

Slope–shelf and ridge regions are the sites of complex frontal and current systems at which the incident waves are refracted and scattered. We completely ignored this complex environment and replaced it by an ocean where the BV frequency varies neither vertically nor horizontally and where there are no mean flows.

A third major idealization is that we consider free, linear, and undamped waves, not affected by forcing, nonlinear interactions, and dissipative processes. We have taken this point into account by applying our theory only to the lowest 60 modes, which are not as severely affected by theses processes as higher modes. The higher modenumber resolution for the scattered waves was implemented for computational reasons. This restriction of course leaves out a substantial part of the internal wave field, especially the part that carries the shear. We have also assumed that the incoming wave field is a superposition of statistically independent plane waves and did not consider the scattering of wave packets or other wave forms.

Despite all these idealizations we believe that our results are applicable to the real ocean, especially when we compare different topographic profiles. These results are the following.

- At frequencies lower than the critical frequency most of the incident flux is reflected back. At frequency higher than the critical frequency most of the incident flux is transmitted onto the shelf or across the ridge. The topography thus acts like a filter in frequency space. Since typical topographic slopes imply a critical frequency close to the Coriolis frequency, this

filtering leads to an elimination of the inertial peak for slope spectra.

- Both the reflected and transmitted modenumber spectra are flatter than the incident spectrum. This implies a redistribution of the incident flux from low to high modenumbers. This is presumably a statistical tendency, an approach towards statistical equilibrium.
- The transfer to high modenumbers is accompanied by an amplification of the energy level and, even more so, of the shear level.
- The energy flux to modenumbers higher than the critical modenumber, that is, to waves that are likely to break and cause mixing, depends on the topographic profile. Convex profiles are more efficient than linear and concave profiles.

Overall, our calculations indicate that the scattering at topography causes a significant distortion to the incident Garrett and Munk spectrum, and these distortions will induce a variety of dynamical adjustment processes. Topography is thus a dynamically active area for internal waves.

APPENDIX

Garrett–Munk Spectrum (GM79)

In this paper we use the GM spectrum given in Munk (1981). It is also referred to as GM79. It is explicitly given by

$$E_{GM}(\omega, n, z) = b^2 N(0) N(z) E_{GM}(\omega, n), \quad (A1)$$

with

$$N(z) = N(0)e^{z/b}$$

$$E_{GM}(\omega, n) = E_0 B(\omega) H(n)$$

$$B(\omega) = \frac{2f}{\pi\omega} \frac{1}{\sqrt{\omega^2 - f^2}}$$

$$H(n) = \frac{(n^2 + n_*^2)^{-1}}{\sum\limits_{1}^{\infty} (n^2 + n_*^2)^{-1}}. \quad (A2)$$

The parameters are

$$b = 1.3 \text{ km} \qquad N(0) = 5.2 \times 10^{-3} \text{ s}^{-1} \text{ (3 cph)}$$

$$n_* = 3 \qquad E_0 = 6.3 \times 10^{-5}. \quad (A3)$$

For modenumber n, the horizontal wavenumber k and vertical wavenumber m are determined by

$$k = \frac{n\pi}{b} \sqrt{\frac{\omega^2 - f^2}{N(0)^2 - \omega^2}} \qquad m = \frac{n\pi}{b} \sqrt{\frac{N^2 - \omega^2}{N(0)^2 - \omega^2}}. \quad (A4)$$

REFERENCES

Baines, P. G., 1971a: The reflexion of internal/inertial waves from bumpy surfaces. *J. Fluid Mech.,* **46,** 273–291.
——, 1971b: The reflexion of internal/inertial waves from bumpy surfaces. Part 2: Split reflexion and diffraction. *J. Fluid Mech.,* **49,** 113–131.
——, 1973: The generation of internal tides by flat bumpy topography. *Deep-Sea Res.,* **20,** 179–205.
Cacchione, D., and C. Wunsch, 1974: Experimental study of internal waves over a slope. *J. Fluid Mech.,* **66,** 223–239.
D'Asaro, E., 1991: A strategy for investigating and modeling internal wave sources and sinks. *Dynamics of Oceanic Internal Gravity Waves,* P. Müller and D. Henderson, Eds., 'Aha Huliko'a Hawaiian Winter Workshop Series, SOEST Special Publ., 451–465.
Eriksen, C. C., 1982: Observations of internal wave reflection off sloping bottoms. *J. Geophys. Res.,* **87,** 525–538.
——, 1985: Implication of ocean bottom reflections for internal wave spectra and mixing. *J. Phys. Oceanogr.,* **15,** 1145–1156.
——, 1998: Internal wave reflection and mixing at Fieberling Guyot. *J. Geophys. Res.,* **103,** 2977–2994.
Garrett, C., and W. Munk, 1972: Space–time scales of internal waves. *Geophys. Fluid Dyn.,* **2,** 225–264.
——, and D. Gilbert, 1988: Estimates of vertical mixing by internal waves reflected off a sloping bottom. *Small-Scale Turbulence and Mixing in the Ocean,* J. C. J. Nihoul and B. M. Jamard, Eds., Elsevier Scientific, 405–424.
Gilbert, D., and C. Garrett, 1989: Implications for ocean mixing of internal waves scattering off irregular topography. *J. Phys. Oceanogr.,* **19,** 1716–1729.
Ivey, G. N., and R. I. Nokes, 1989: Mixing driven by the breaking of internal waves against sloping boundaries. *J. Fluid Mech.,* **204,** 479–500.
Müller, P., and N. Xu, 1992: Scattering of oceanic internal gravity waves off random bottom topography. *J. Phys. Oceanogr.,* **22,** 474–488.
——, and X. Liu, 2000: Scattering of internal waves at finite topography in two dimensions. Part I: Theory and case studies. *J. Phys. Oceanogr.,* **30,** 532–549.
Munk, W., 1981: Internal waves and small scale processes. *Evolution of Physical Oceanography,* B. A. Warren and C. Wunsch, Eds., The MIT Press, 264–291.
Phillips, O. M., 1966: *The Dynamics of the Upper Ocean.* Cambridge University Press, 336 pp.
Rubenstein, D., 1988: Scattering of inertial waves by rough bathymetry. *J. Phys. Oceanogr.,* **18,** 5–18.
Sandstrom, H., 1976: On topographic generation and coupling of internal waves. *J. Fluid Dyn.,* **7,** 231–270.